JACS
JOURNAL OF THE AMERICAN CHEMICAL SOCIETY

Article

pubs.acs.org/JACS

Engineering Intracellular Delivery Nanocarriers and Nanoreactors from Oxidation-Responsive Polymersomes via Synchronized Bilayer Cross-Linking and Permeabilizing Inside Live Cells

Zhengyu Deng,[†] Yinfeng Qian,[‡] Yongqiang Yu,[‡] Guhuan Liu,[†] Jinming Hu,[†] Guoying Zhang,[†] and Shiyong Liu*[,†]

[†]CAS Key Laboratory of Soft Matter Chemistry, Hefei National Laboratory for Physical Sciences at the Microscale, *i*ChEM (Collaborative Innovation Center of Chemistry for Energy Materials), Department of Polymer Science and Engineering, University of Science and Technology of China, Hefei, Anhui 230026, China

[‡]Department of Radiology, The First Affiliated Hospital of Anhui Medical University, Hefei, Anhui 230022, China

Supporting Information

ABSTRACT: Reactive oxygen species (ROS) and oxidative stress are implicated in various physiological and pathological processes, and this feature provides a vital biochemical basis for designing novel therapeutic and diagnostic nanomedicines. Among them, oxidation-responsive micelles and vesicles (polymersomes) of amphiphilic block copolymers have been extensively explored; however, in previous works, oxidation by ROS including H_2O_2 exclusively leads to microstructural destruction of polymeric assemblies. For oxidation-responsive polymersomes, fast release of encapsulated hydrophilic drugs and bioactive macromolecules will occur upon microstructural disintegration. Under certain application circumstances, this does not meet design requirements for sustained-release drug nanocarriers and long-acting in vivo nanoreactors. Also note that conventional polymersomes possess thick hydrophobic bilayers and compromised membrane permeability, rendering them as ineffective nanocarriers and nanoreactors. We herein report the fabrication of oxidation-responsive multifunctional polymersomes exhibiting intracellular milieu-triggered vesicle bilayer cross-linking, permeability switching, and enhanced imaging/drug release features. Mitochondria-targeted H_2O_2 reactive polymersomes were obtained through the self-assembly of amphiphilic block copolymers containing arylboronate ester-capped self-immolative side linkages in the hydrophobic block, followed by surface functionalization with targeting peptides. Upon cellular uptake, intracellular H_2O_2 triggers cascade decaging reactions and generates primary amine moieties; prominent amidation reaction then occurs within hydrophobic bilayer membranes, resulting in concurrent cross-linking and hydrophobic-to-hydrophilic transition of polymersome bilayers inside live cells. This process was further utilized to achieve integrated functions such as sustained drug release, (combination) chemotherapy monitored by fluorescence and magnetic resonance (MR) imaging turn-on, and to construct intracellular fluorogenic nanoreactors for cytosolic thiol-containing bioactive molecules.

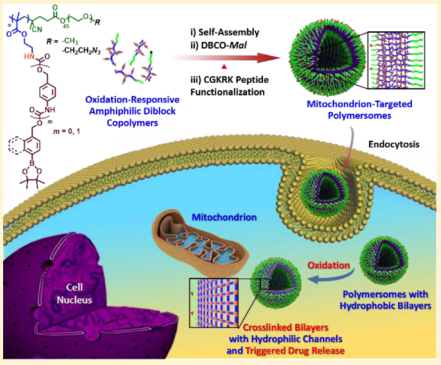

INTRODUCTION

In living organisms, reactive oxygen species (ROS) are persistently generated, transformed, and consumed. They play crucial roles in various physiological processes such as cellular growth, signaling, immune response, and senescence.[1] Importantly, oxidative stress from acute and chronic over-production and accumulation of ROS can cause a variety of types of diseases including cancer, ischemia/reperfusion, inflammation, neurodegenerative diseases, and so forth.[2] As one of the most abundant and stable forms of ROS, hydrogen peroxide (H_2O_2), which is freely diffusible within and between cells, is endogenously generated within cell membranes, mitochondria, endoplasmic reticulum, and phagosomes. Elevated generation rates of H_2O_2 are typically found in most types of cancer cells (up to ~0.5 nmol/10^4 cells/h),[3] monocytes, and stimulated polymorphonuclear leukocytes (up to ~1.5 nmol/10^4 cells/h).[4] In most cases, biologically relevant equilibrium H_2O_2 levels are very low (50−200 μM),[5] although recent reports showed that H_2O_2 levels in phagosomes within dendritic cells (DCs), that is, the most effective antigen-presenting cells (APCs), could be up to 1 mM.[6] This feature provides a vital biochemical basis for designing novel types of diagnostic/therapeutic agents and smart nanocarriers, which exploit abnormal oxidative milieu to achieve selective activation and targeted delivery of drugs, proteins, and imaging agents.[7]

For micelles and vesicles (or polymersomes) self-assembled from amphiphilic block copolymers (BCPs),[8] endowing them with responsiveness toward externally applied stimuli or endogenous stimuli associated with pathological sites (e.g., low pH, enzymes, and oxidative stress) could enable the "sense-and-act" module for "on-demand" drug release in a

Received: April 22, 2016
Published: August 3, 2016

DOI: 10.1021/jacs.6b04115
J. Am. Chem. Soc. 2016, 138, 10452−10466

Scheme 1. Schematics for the Fabrication of Oxidation-Responsive Multifunctional Polymersomes Exhibiting Intracellular Milieu-Triggered Vesicle Bilayer Cross-Linking, Permeability Switching, and Enhanced Imaging/Drug Release Features[a]

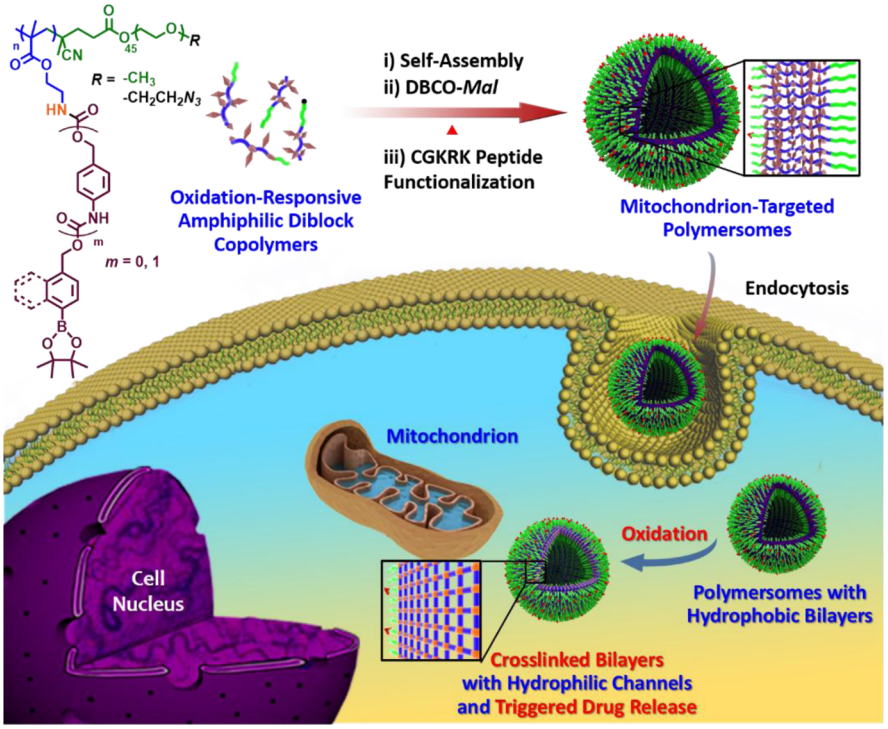

[a]Mitochondria-targeted reactive polymersomes were obtained through the self-assembly of amphiphilic BCPs containing arylboronate ester-capped self-immolative side linkages in the hydrophobic block, followed by surface functionalization with targeting peptides. Upon cellular uptake, mitochondrial H_2O_2 triggers cascade decaging reactions and releases primary amine moieties; a prominent amidation reaction then occurs due to suppressed amine pK_a within hydrophobic membranes, resulting in concurrent cross-linking and hydrophobic-to-hydrophilic transition of polymersome bilayers inside live cells. This process was further utilized to construct intracellular nanoreactors and achieve integrated functions such as combination chemotherapy guided by fluorescence and MR imaging turn-on features.

spatiotemporal and dosage-controlled manner.[9] In contrast to BCP micelles, polymersomes could encapsulate both hydrophobic substances (typically of low molecular weight, MW) and hydrophilic payloads ranging from low to ultrahigh MW species (e.g., antibiotics, drugs, peptides/proteins/enzymes, and therapeutic nucleic acids).[10] Thus, they have been extensively utilized to construct drug delivery nanocarriers,[11] biomimetic organelles,[12] and artificial nanoreactors.[13]

Previous reports concerning oxidation-responsive polymeric assemblies mainly focused on micellar nanoparticles,[14] whereas H_2O_2-responsive polymersomes have been far less explored.[15] It is worth noting that in all of these cases, H_2O_2 oxidation exclusively led to microstructural destruction and disintegration of polymeric micelles and vesicles. For H_2O_2-responsive polymersomes, fast release of loaded hydrophilic drugs and bioactive species will occur upon disruption of microstructural integrity. Under certain application circumstances, this does not meet the design requirements for sustained-release drug nanocarriers and long-acting in vivo nanoreactors over extended periods.[13] Thus, the design of oxidation-responsive polymersomes capable of retaining vesicular integrity is to be solved.

On the other hand, conventional nonresponsive polymersomes suffer from severe permeability issues due to thick hydrophobic bilayers, which are almost impermeable toward small molecules, ions, and even water molecules.[16] To maintain structural integrity of polymersomes, chemical cross-linking strategies have been traditionally utilized; however, this process typically leads to further compromised bilayer permeability.[17] Thus, it is highly desirable to construct oxidation-responsive polymersomes with both H_2O_2-switchable bilayer permeability and superior structural stability.[18] The former aspect could avoid premature drug release during blood circulation and promote selective release at disease sites expressing high H_2O_2 levels, and the latter could enable the construction of long-term stable intracellular nanoreactors and sustained-release nanocontainers. However, to the best of our knowledge, these features have not yet been achieved for oxidation-responsive polymersomes.

In addition, previously reported examples of H_2O_2-responsive polymersomes worked in the H_2O_2 range of 9 mM to 3.3 M,[15] which are less relevant to biological H_2O_2 levels. Previously, Chang et al.[19] and Kim et al.[20] reported the construction of luminescent H_2O_2 probes and H_2O_2-activatable theranostic prodrugs based on bioorthogonal H_2O_2 oxidation of small molecule arylboronate derivatives. In the pioneering work of Fréchet and co-workers,[14a] they fabricated polymeric nanoparticles of phenylboronic ester-modified dextran, which sensitively respond to H_2O_2 with a concentration down to ~1 mM. Later, Almutairi et al.[14d,21] reported oxidation-responsive polyester nanoparticles capable of backbone cleavage in response to ~100 μM H_2O_2 levels. In 2011, we reported the fabrication of optical H_2O_2 probes with the detection limit down to ~20 μM based on charge-generation polymers (CGPs) containing phenylboronic ester moieties.[22] Most recently, we designed hyperbranched self-immolative polymers

DOI: 10.1021/jacs.6b04115
J. Am. Chem. Soc. 2016, 138, 10452−10466

(*h*SIPs) with H_2O_2-reactive phenylboronate trigger installed at the focal point; the fluorogenic H_2O_2 detection limit could be further down to ~20 nM.[23]

Motivated by the above designs and in view of our previous works[18c] concerning UV light-induced "traceless" cross-linking of polymersome bilayers with concomitant membrane polarity shifting, we herein report the fabrication of oxidation-responsive multifunctional polymersomes exhibiting intracellular milieu-triggered cross-linking of vesicle bilayers, permeability switching, and enhanced imaging/drug release features (Scheme 1). During optimization of the chemical design in terms of self-assembling nanostructure morphologies and H_2O_2 response rates, we mainly screened two types of arylboronate derivatives, phenylboronate (PB) and naphthylboronate (NB) esters, and self-immolative linkers of varying spacer lengths (Scheme 2).[24] Starting from four types of H_2O_2-responsive monomers, PBMA, PBCMA, NBMA, and NBCMA, it was found that among all sample series synthesized, only PEO-*b*-PNBMA BCPs could reliably self-assemble into vesicles or large compound vesicles (LCVs; Table 1). Mitochondria-targeted H_2O_2-reactive polymersomes were then obtained via surface functionalization of PEO-*b*-PNBMA vesicles with targeting peptides. Upon cellular uptake, intracellular H_2O_2 triggers removal of NB capping moieties, followed by self-immolative decaging reactions and generation of primary amine moieties. Extensive amidation reactions then occur due to elevated effective molarity and suppressed amine pK_a within hydrophobic bilayer membranes and the equilibrium nature of amine protonation/deprotonation, resulting in synchronized bilayer cross-linking and hydrophobic-to-hydrophilic transition of bilayer membranes inside the milieu of live cells. This process was further integrated to construct sophisticated functions such as combination chemotherapy guided by fluorescence and magnetic resonance (MR) imaging turn-on features. On the basis of endogenous H_2O_2-triggered polymersome cross-linking and bilayer permeability switching, we further demonstrate the fabrication of highly stable intracellular fluorogenic nanoreactors selectively for cytosolic thiol-containing bioactive molecules (Scheme 1).

Scheme 2. Synthetic Routes Employed for the Preparation of Oxidation-Responsive Monomers and Amphiphilic Diblock Copolymers Containing Self-Immolative Carbamate Side Linkages in the Hydrophobic Block

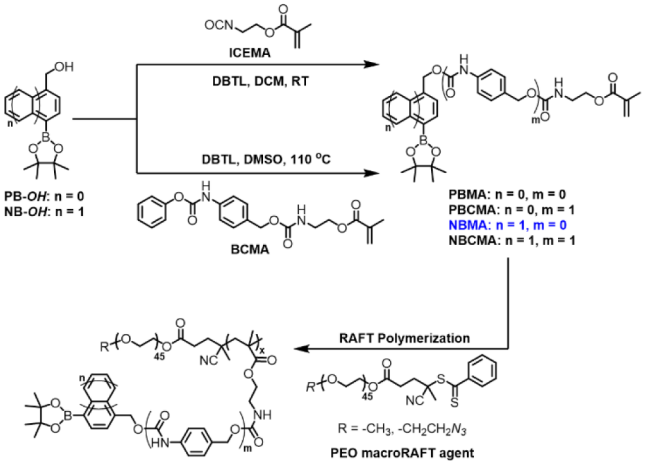

RESULTS AND DISCUSSION

Synthesis and Supramolecular Self-Assembly of Oxidation-Responsive Amphiphilic Block Copolymers. To reliably and reproducibly fabricate polymersomes via controlled self-assembly of H_2O_2-responsive BCPs with appropriate chemical structures is a prerequisite. On the basis of recent works, we have realized that synergistic noncovalent interactions such as hydrophobic, hydrogen bonding, $\pi-\pi$ stacking, and paired electrostatic (zwitterionic) interactions within the hydrophobic block could considerably promote and stabilize the formation of higher-order nanostructures (e.g., vesicles, LCVs, circular disks, and staggered lamellae) other than spherical micelles, even for amphiphilic BCPs with relatively low hydrophobic-to-hydrophilic block length ratios.[18c,25] We started with the synthesis of PBMA monomer, which contains carbamate-caged primary amine and H_2O_2-reactive capping moiety, from 4-hydroxy(methyl)-phenylboronic acid pinacol ester, PB-*OH*, and isocyanate-containing monomer, ICEMA (Scheme 2).[22] Reversible addition−fragmentation chain transfer (RAFT) polymerization of PBMA was conducted using PEO_{45}-based macroRAFT agent, affording a series of amphiphilic BCPs with varying hydrophobic block lengths, PEO_{45}-*b*-$PPBMA_n$ (n = 15, 35, and 53). However, all three BCPs could only self-assemble into micellar nanoparticles (representative data of PEO_{45}-*b*-$PPBMA_{15}$, **P1**, shown in Figure S1d and Table 1), which seems to be independent of self-assembling conditions (e.g., water addition rate and cosolvent).

Table 1. Structural Parameters of Oxidation-Responsive Amphiphilic BCPs Synthesized in This Work

entry	samples	$M_{n,NMR}$ (kDa)[a]	$M_{n,GPC}$ (kDa)[b]	M_w/M_n[b]	$\langle D_h \rangle$ (nm)[c]	nanostructure morphology[d]
N1	PEO_{45}-*b*-$PNBMA_{12}$	7.5	8.6	1.21	70	LCM
N2	PEO_{45}-*b*-$PNBMA_{16}$	9.3	10.7	1.17	510	V
N3	PEO_{45}-*b*-$PNBMA_{26}$	13.7	17.1	1.25	400	LCV
azide-**N4**	N_3-PEO_{45}-*b*-$PNBMA_{16}$	9.5	11.1	1.29	540	V
NC1	PEO_{45}-*b*-$PNBCMA_{16}$	11.7	13.5	1.2	80	LCM
P1	PEO_{45}-*b*-$PPBMA_{15}$	8.1	9.8	1.18	30	M
PC1	PEO_{45}-*b*-$PPBCMA_{15}$	10.3	12.1	1.24	300	LCM
3HF-**N5**	PEO_{45}-*b*-$P(NBMA_{0.98}$-*co*-$3HFM_{0.02})_{16}$	9.3	10.5	1.27	500	V
CM-**N6**	PEO_{45}-*b*-$P(NBMA_{0.95}$-*co*-$CMA_{0.05})_{16}$	9.2	10.6	1.19	520	V
FMA-**N7**	PEO_{45}-*b*-$P(NBMA_{0.99}$-*co*-$FAEMA_{0.01})_{16}$	9.3	11.2	1.15	530	V
Gd-**N8**	PEO_{45}-*b*-$P(NBMA_{0.94}$-*co*-$Gd_{0.06})_{16}$		11.1	1.22	490	V

[a]Calculated from ^{1}H NMR results. [b]Determined by GPC using THF as the eluent. [c]Determined by dynamic laser light scattering (DLS). [d]Determined by TEM and SEM (M = micelles; V = vesicles; LCV = large compound vesicles; LCM = large compound micelles).

DOI: 10.1021/jacs.6b04115
J. Am. Chem. Soc. 2016, 138, 10452−10466

We then speculated that the incorporation of one additional self-immolative *p*-aminobenzyl carbamate linker into PBMA, that is, the PBCMA monomer, will enhance hydrogen bonding and $\pi-\pi$ stacking interactions among hydrophobic segments due to the presence of two carbamate and two benzyl moieties (Scheme 2). This should help promote the formation of higher-order nanostructures.[18c,25] Also note that polymeric blocks of PBMA and PBCMA possess different side chain spacer lengths (m = 0, 1), and they should exhibit varying self-immolative decaging kinetics.[24] PBCMA monomer was synthesized from PB-*OH* and BCMA bearing latent isocyanate functionality (Scheme 2).[25e] Unfortunately, corresponding PEO_{45}-*b*-$PPBCMA_n$ (n = 15, 25, and 48) BCPs could still only self-assemble into spherical large compound micelles (representative data of PEO_{45}-*b*-$PPBCMA_{15}$, **PC1**, shown in Figure S1e and Table 1).

Considering that arylboronate derivatives with more extended π-conjugation such as *NB*-OH[26] should further enhance $\pi-\pi$ stacking noncovalent interactions and might also exhibit distinct H_2O_2 oxidation kinetics, we attempted the synthesis of NBMA and NBCMA monomers via the reaction of NB-*OH* with ICEMA and BCMA, respectively (Scheme 2). Next, a series of PEO_{45}-*b*-$PNBMA_n$ (**N1**, **N2**, and **N3**; Table 1) and PEO_{45}-*b*-$PNBCMA_n$ (n = 16, **NC1**; Table 1) BCPs with varying hydrophobic block lengths were synthesized via RFAT polymerizations (Scheme 2). It was found that by using 1,4-dioxane as the cosolvent, **N2** and **N3** could self-assemble in aqueous media into polymersomes and large compound vesicles, respectively, as confirmed by transmission electron microscopy (TEM) and scanning electron microscopy (SEM) observations (Figure 1a,c; Figures S1b and S2; Table 1). On the other hand, **N1** and **NC1** could self-assemble into large compound micelles (LCMs) (Figure S1a,c; Table 1). Note that all intermediate compounds, monomers, and BCPs were fully characterized by ^1H and ^{13}C NMR, ESI−MS, and GPC analysis (see Figures S3−S7 for details). Table 1 summarizes the structural parameters of all oxidation-responsive BCPs synthesized in this work, along with intensity-average hydrodynamic diameters, $\langle D_h \rangle$, and corresponding morphologies of self-assembled nanostructures.

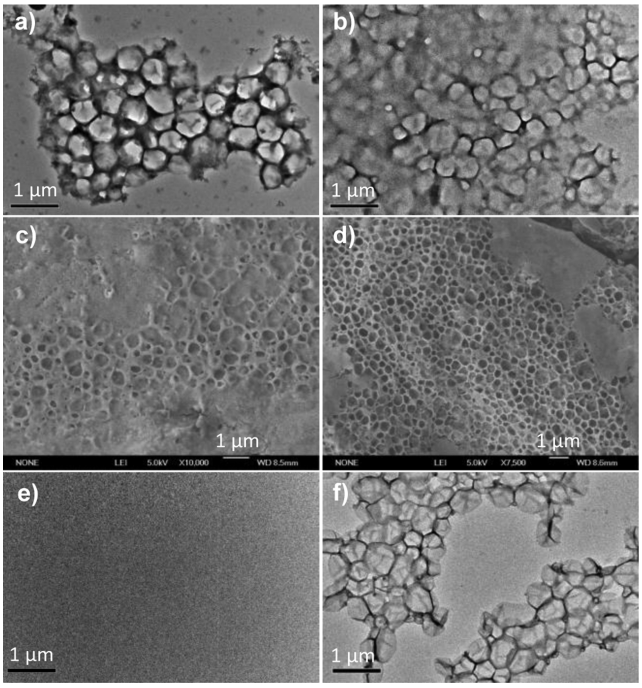

Figure 1. Microscopic characterization of polymeric assemblies before and after incubating with H_2O_2. (a,b) TEM images and (c,d) SEM images of **N2** vesicles (0.1 g/L) (a,c) before and (b,d) after incubation with H_2O_2 (1 mM) for 12 h in PBS buffer (pH 7.4, 10 mM). (e,f) TEM images of **N2** vesicles (0.1 g/L) after 12 h incubation in the (e) absence and (f) presence of 1 mM H_2O_2 in PBS buffer (pH 7.4, 10 mM), respectively, followed by 19-fold dilution with DMF.

To enable surface decoration with mitochondria-targeting peptides, azide-terminated BCP, N_3-PEO_{45}-*b*-$PNBMA_{16}$ (*azide*-**N4**; Table 1), was synthesized via RAFT polymerization using azide-anchored PEO_{45}-based macroRAFT agent. Oxidation-responsive BCPs covalently labeled with fluorescent 3-hydroxyflavone (*3HF*-**N5**) probe and fluorescein isothiocyanate (FITC; *FMA*-**N7**), or fluorogenic coumarin moieties (*CM*-**N6**; Scheme S2a and Figure S8), were also synthesized. The chemical structures of *3HF*-**N5**, *CM*-**N6**, and *FMA*-**N7** BCPs are shown in Scheme S1, and their structural parameters are summarized in Table 1. Amphiphilic BCP with the hydrophobic oxidation-responsive block covalently conjugated with Gd complexes, DOTA-*Gd*, for magnetic resonance (MR) imaging contrast enhancement, *Gd*-**N8**, was also synthesized via RAFT copolymerization and postmodification (Scheme S2b and Figure S9; Table 1). Importantly, the formation of vesicular assemblies remains to be unaffected by either the alteration of PEG terminal functionality (methoxyl versus azido) or covalent conjugation of fluorescent dyes (3HF, CM, and FMA) and MR imaging contrast agent (DOTA-*Gd*) onto the oxidation-responsive block (Table 1 and Figure S1f).

H_2O_2-Triggered Synchronized "Traceless" Cross-Linking and Bilayer Permeability Switching of Oxidation-Responsive Vesicles. All four types of amphiphilic BCPs (i.e., PEO-*b*-PPBMA, PEO-*b*-PPBCMA, PEO-*b*-PNBMA, and PEO-*b*-PNBCMA) contain either PB ester or NB ester moieties (Scheme 2). Thus, both of them are expected to inherit H_2O_2-responsiveness, just as their small molecule counterparts. Our general design is that upon H_2O_2-triggered cleavage of PB and NB capping moieties, subsequent cascade self-immolative decaging reactions will lead to generation of the same poly(2-aminoethyl methacrylate) (PAEMA) scaffold for all four types of BCPs. Newly generated primary amines possess several reaction pathways including single/double addition reactions with quinone methide intermediates, protonation, and intra-chain and interchain amidation reactions; note that the latter could lead to chemical cross-linking of vesicle bilayers (Schemes 1 and 3).[18c,25e]

Taking **N2** polymersomes as a prototype, we examined at first the reactivity of both NBMA and **N2** polymersomes toward H_2O_2. As expected, H_2O_2 reactivity of **N2** was not compromised after polymerization of NBMA and self-assembly. In the presence of 1 mM H_2O_2, the absorbance peak of NBMA monomer centered at ~297 nm progressively decreased, whereas a new absorbance peak at ~328 nm intensified within ~8 h incubation time (Figure S10a). This should be ascribed to the oxidation of NB moieties and generation of 4-(hydroxymethyl)-1-naphthol (HMN) from the reaction of quinone methide intermediates with water (Scheme 3 and Figure S11). H_2O_2 oxidation of N2 polymersome dispersion led to more prominent absorbance band changes (Figure S10b), and a longer incubation duration was necessary for the reaction to complete. The apparently different extents of absorbance band changes between NBMA monomer and N2 polymer-

DOI: 10.1021/jacs.6b04115
J. Am. Chem. Soc. 2016, 138, 10452−10466

Scheme 3. Schematics of Cascade Events upon H_2O_2 Oxidation of Polymeric Assemblies[a]

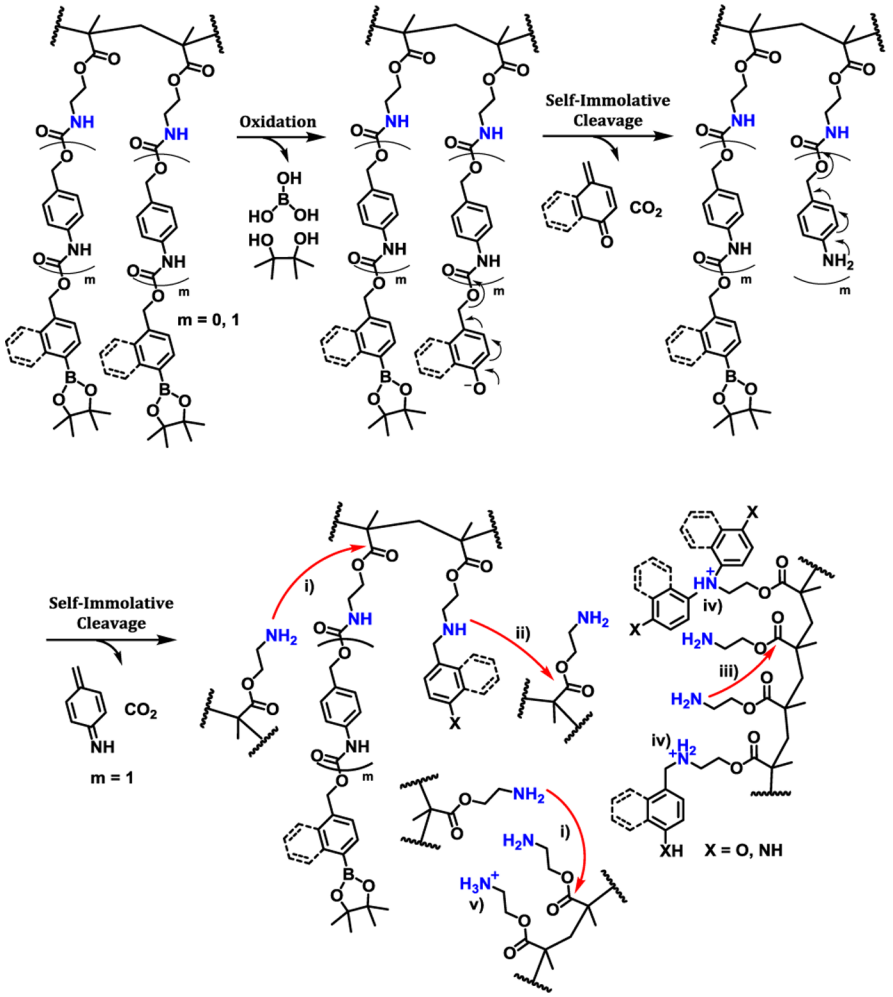

[a]Oxidation-triggered decaging of boronic ester capping moieties leads to spontaneous self-immolative cleavage and release of primary amine functionalities; prominent amidation reactions then occur, leading to cross-linking of polymeric assemblies (mainly contributed by interchain amidation reactions). Annotation: (i,ii) interchain amidation reactions of (i) primary amines and (ii) secondary amines generated by reacting with quinone methide intermediates; (iii) intrachain amidation reactions; (iv) protonated secondary and tertiary amines generated via single and double reactions of primary amines with quinone methide intermediates, respectively; and (v) protonated primary amines unreactive towards amidation reactions.

somes upon H_2O_2 oxidation could be ascribed to different reaction pathways of quinone methide intermediates, that is, exclusive HMN formation in the former (Figure S11), and generation of HEAMN, HMN, HEA$(MN)_2$, and other minor products in the latter case (see Figure S19 for details); note that reaction conditions (DMSO/PBS buffer 97/3 v/v mixture vs PBS buffer) and concentration differences (0.12 mM vs 0.17 mM NBMA moieties) might further contribute toward this aspect. Most importantly, other intracellular bioactive molecules such as glutathione (GSH) and typical ROS species including hydroxyl radical (·OH), *tert*-butoxy radical (·OtBu), hypochlorite (OCl^-), and *tert*-butyl hydroperoxide (TBHP) could not lead to effective **N2** oxidation (Figure S12). These results supported superior selectivity and sensitivity of arylboronate moieties toward H_2O_2 as compared to diselenium[14c] and thioether[15b] moieties, which augurs well for the application of arylboronate-based oxidation-responsive vesicles within intracellular milieu.

Next, we further examined H_2O_2-responsive properties of **N2** polymersomes by dynamic light scattering (DLS) technique. Prior to H_2O_2 addition, **N2** vesicle dispersion (pH 7.4, 25 °C) exhibited a $\langle D_h \rangle$ of ∼510 nm and a size polydispersity (μ_2/Γ^2) of ∼0.178 (Figure 2a). The scattering intensity exhibited negligible changes after 12 h incubation without H_2O_2, suggesting that **N2** polymersomes are resistant to spontaneous hydrolysis in aqueous milieu (Figure 2b). In contrast, in the presence of 1 mM H_2O_2, $\langle D_h \rangle$ slightly increased from ∼510 to ∼530 nm after 12 h incubation, while scattering light intensities exhibited a ∼ 33% decrease within the same incubation duration. These results are also consistent with time-dependent UV/vis absorbance results (Figure S10). For micellar nanoparticles self-assembled from **NC1**, **P1**, and **PC1** amphiphilic BCPs, both scattering light intensity and $\langle D_h \rangle$ follow trends similar to those of **N2** polymersomes upon H_2O_2 coincubation, that is, a modest decrease of scattering intensities and a slight increase of $\langle D_h \rangle$ over the whole incubation period (Figure S13a−c). These results clearly confirmed that the H_2O_2-reactive feature of arylboronate moieties was retained for polymeric assemblies of all four types of amphiphilic BCPs (Scheme 1).

DOI: 10.1021/jacs.6b04115
J. Am. Chem. Soc. 2016, 138, 10452−10466

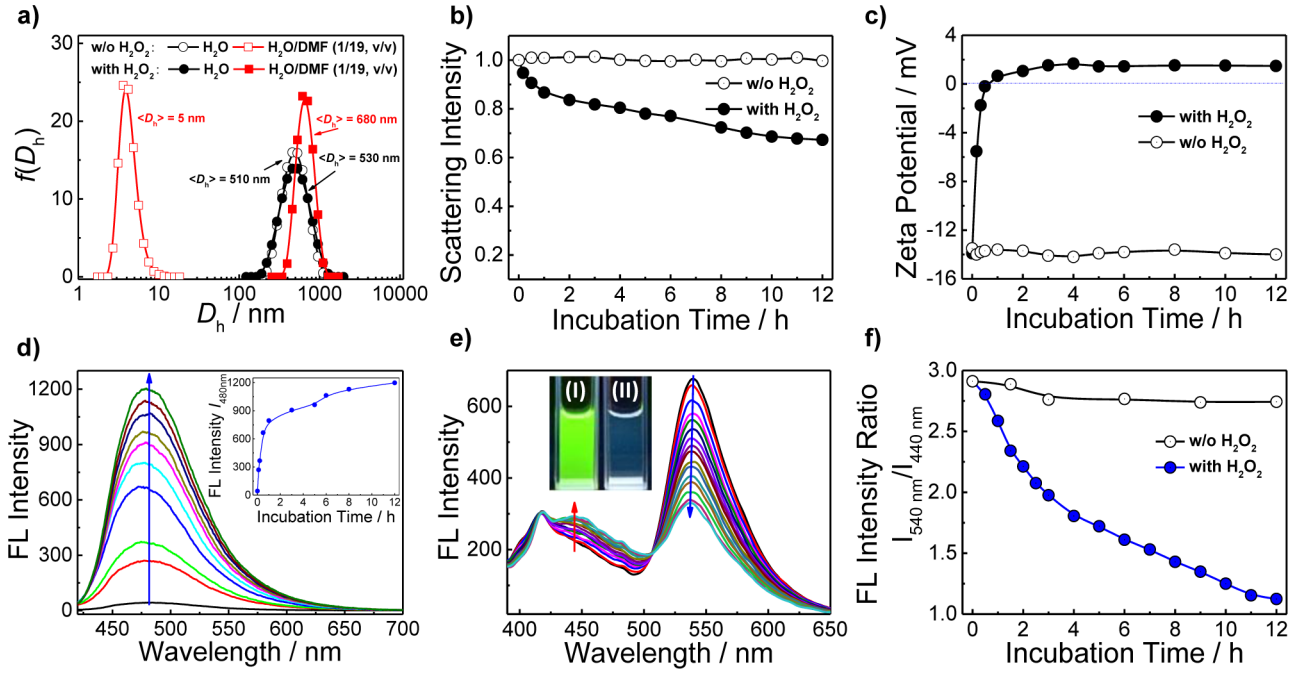

Figure 2. Characterization of **N2** and *3HF*-**N5** polymersomes (0.1 g/L) upon incubation with H_2O_2 (1 mM; PBS buffer, pH 7.4, 10 mM; 25 °C). (a) Intensity-average hydrodynamic diameter distributions, $f(D_h)$, recorded for **N2** polymersome dispersions with and without H_2O_2 treatment for 12 h, followed by 19-fold dilution with DMF and water, respectively. (b,c) Incubation duration-dependent evolution of (b) normalized scattering light intensity and (c) zeta potential of **N2** polymersome dispersion without or with H_2O_2 addition. (d) Time-dependent evolution of fluorescence emission spectra (λ_{ex} = 390 nm) recorded for **N2** polymersome dispersions upon incubation with H_2O_2, followed by reacting with fluorescamine (FA). The inset in (d) shows incubation time-dependent changes in FA emission intensities at 480 nm. (e) Evolution of fluorescence emission spectra (λ_{ex} = 365 nm) of *3HF*-**N5** polymersome dispersion upon H_2O_2 addition. (f) Time-dependent evolution of emission intensity ratios, $I_{540\ nm}/I_{440\ nm}$, of *3HF*-**N5** polymersome dispersion without and with H_2O_2 addition. The inset in (e) shows macroscopic images recorded under UV 365 nm irradiation for *3HF*-**N5** polymersome dispersion after incubation in the (I) absence and (II) presence of H_2O_2 for 12 h.

Closer examination of Figure S13a revealed that supramolecular assemblies of **P1**, **PC1**, **N2**, and **NC1** with comparable responsive/hydrophobic block lengths (degree of polymerization, DP ≈ 15−16) possess varying response rates toward H_2O_2, with relative rates in the order of **P1** > **PC1** > **N2** > **NC1**. Note that H_2O_2 response rates are dependent on the types of capping agents (PB/NB) and the length of self-immolative side linkages (m = 0, 1; Schemes 1 and 2). Recently, Gillies et al.[27] reported that the depolymerization rate of self-immolative linear polymers with precise DPs is solely dependent on chain lengths. It is then reasonable to infer that H_2O_2 response rates of **PC1** and **NC1** assemblies are lower than those of **P1** and **N2** assemblies, respectively. With the length of self-immolative side linkages being the same, PB capping moieties react faster with H_2O_2 than NB ones, perhaps due to extended π-conjugated nature of the latter.[26] Taken together, the observed order of H_2O_2 response rates for polymeric assemblies of **P1**, **PC1**, **N2**, and **NC1** could be well interpreted.

We then utilized physically encapsulated Nile red (NR) to probe changes in microenvironmental polarity for oxidation-responsive polymersomes and micelles (Figure S13d). Note that as a hydrophobic fluorescent probe, NR is intensely fluorescent within hydrophobic milieu and weakly fluorescent in hydrophilic milieu. It was found that **N2** polymersomes and micelles of **P1**, **PC1**, and **NC1** all underwent prominent shift from hydrophobicity to hydrophilicity upon treating with H_2O_2. As expected, both **P1** and **N2** assemblies exhibited faster changes in microenvironmental polarity as compared to those of **PC1** and **NC1**, respectively. Intriguingly, after extended coincubation with H_2O_2, the final equilibrium NR emission intensities of **P1** micelles and **PC1** micelles are quite comparable to those of **N2** polymersomes and **NC1** micelles, respectively (Figure S13d).

For **N2** vesicles, although a significant hydrophobic-to-hydrophilic transition occurs within vesicle bilayers upon H_2O_2 treating for 12 h, vesicular nanostructures were well retained, as confirmed by both TEM and SEM observations (Figure 1b,d). These results are also in agreement with those of DLS measurements (Figure 2a,b). To clarify the apparent dilemma between drastically enhanced hydrophilicity (Figure S13d) and the maintaining of vesicular nanostructures after H_2O_2 coincubation, additional experiments were then conducted. First, the zeta potential of **N2** vesicle dispersion initially increased from ca. −14 to ca. +1.5 mV and then almost leveled off after ∼2 h of H_2O_2 incubation (Figure 2c), suggesting the generation of positively charged species on the polymersome scaffolds upon H_2O_2 incubation. Negligible changes in zeta potential were observed in the absence of H_2O_2 addition, which is in accordance with the stability of **N2** polymersomes against spontaneous hydrolysis (Figure 2b). Note that NB capping moieties are expected to be oxidized in the presence of H_2O_2 with the liberation of primary amines after cascade 1,6-elimination and decarboxylation events (Scheme 3). The generation of primary amines was further verified by using fluorescamine (FA) as a fluorogenic probe, which is initially nonfluorescent but rendered intensely fluorescent after reacting with primary amines (Figure 2d).

UV/vis absorbance data (Figure S10b) revealed that oxidation of NB moieties in **N2** continuously occurred within

DOI: 10.1021/jacs.6b04115
J. Am. Chem. Soc. 2016, 138, 10452−10466

0−10 h incubation after H_2O_2 addition, suggesting that more primary amines should be generated at extended incubation time. However, the zeta potential of **N2** vesicle dispersion remained almost constant after ∼2 h H_2O_2 coincubation (Figure 2c). As compared to the nontreated control, the retaining of vesicular nanostructures after 12 h of H_2O_2 treatment followed by 19-fold dilution with DMF implied that cross-linking reactions occurred, with underlying mechanisms to be further elucidated (Figure 1e,f and Figure 2a). As depicted in Scheme 3, for newly generated primary amines after H_2O_2 oxidation and spontaneous cascade decaging, they will either be protonated or remain in the deprotonated state, and the protonation/deprotonation equilibrium depends on the apparent pK_a. Importantly, several reaction pathways exist for primary amines in the deprotonated form: (a) single addition reactions with quinone methide intermediates, generating secondary amines; and (b) intrachain and interchain amidation reactions with neighboring ester linkages. Note that the above generated secondary amines might partially remain in the protonated state, and deprotonated ones undergo further addition reactions with quinone methide intermediates, affording tertiary amines; intrachain and interchain amidation reactions involving secondary amine moieties might also occur (Scheme 3). In all cases, interchain amidation reactions could contribute to effective vesicle bilayer cross-linking. If we consider one specific interchain amidation reaction, the resultant cross-linker is conjugated via ester linkage and amide linkage onto two different chains, respectively; however, further amidation reaction of the ester linkage by neighboring primary amines emerging from a third chain will generate a new interchain cross-link, but release the previously cross-link as dangling hydrophilic side linkage (i.e., 2-hydroxyethyl amide moieties). Note that the presence of 2-hydroxyethyl amide moieties will also contribute to a hydrophobic-to-hydrophilic transition within cross-linked vesicle bilayers.

For oxidation-generated primary amines within polymersomes, they might also undergo intrachain 5-exoring closure reactions, forming 2-hydroxyethyl amide functionalities. This type of reaction module is well-known for 2-aminoethyl methacrylate (AEMA) small molecule monomer under the deprotonated state.[28] To explore the feasibility of this reaction pathway, we examined ^{1}H NMR spectra of poly(2-aminoethyl methacrylate) ($PAEMA_{62}$) homopolymer when incubated at pH 7.4 and pH 9.0, respectively (Figure S14). It was found that under both pH conditions, PAEMA with a pK_a of ∼7.6 is very stable, and the classical O → N acyl migration reaction (i.e., 5-exo ring closure within the side chain) does not occur. These results also agree with previous literature reports.[28]

To further confirm that amidation reactions have indeed occurred and led to vesicle bilayer cross-linking, the polymersome dispersion was incubated with H_2O_2 for varying time intervals, followed by 19-fold dilution with DMF and DLS measurements. On the basis of the inflection point in the incubation time versus scattering light intensity plot (Figure S15), we could conclude that amidation-actuated chemical cross-linking started to be increasingly prominent after ∼1.8 h of incubation with H_2O_2. We then speculated that during the initial 0−2 h of H_2O_2 treating, it is possible to use GPC to examine the extent of amidation reactions, as interchain amidation will lead to effective chain branching and formation of larger molar mass species. GPC-MALLS results for polymersome dispersions sampled at varying time intervals (0−2 h) upon H_2O_2 incubation are shown in Figure S16. Indeed, amidation-induced chain branching at early stages could be clearly evidenced by GPC peak broadening, appearance of high MW shoulder elution peaks, and shift of these shoulder peaks to higher MWs at extended incubation duration (Figure S16b). In contrast, no prominent changes of GPC elution peaks could be discerned in the absence of H_2O_2 (Figure S16a).

The above results strongly suggested that chemical cross-linking reactions indeed occurred within **N2** polymersome bilayers upon H_2O_2 oxidation. Considering that intrachain and interchain amidation reactions will release 2-hydroxyethylamine (HEA) and NB-caged HEA, we proceeded to quantify the release of small molecule primary amines. Note that NB-caged HEA released from amidation reactions will further transform into HEA upon subsequent oxidation, and HEA primary amines might further react with quinone methide intermediates to generate secondary and tertiary amine moieties. After H_2O_2 oxidation for 12 h, the polymersome dispersion was subjected to ultrafiltration (MWCO 10 kDa), and primary amine contents of the filtrate were quantified by using FA assay, which exclusively reacts with primary amine moieties in a fluorogenic manner (Figure S17). After 12 h of incubation with H_2O_2 for **N2** polymersome dispersion (0.1 g/L), ∼39.7 μM small molecule primary amines (HEA) were generated, corresponding to ∼23.3% of all N-relevant species in the polymersome dispersion.

Furthermore, extensive formation of amide linkages and depletion of ester linkages within **N2** polymersome bilayers upon H_2O_2 oxidation were further verified by ^{1}H NMR, FT-IR, and X-ray photoelectron spectroscopy (XPS) measurements for lyophilized vesicle dispersions after thorough dialysis (Figure S18). In particular, quantitative analysis of XPS core-level N 1s spectrum revealed that after H_2O_2 incubation, the extent of residual protonated amine species (including primary, secondary, and tertiary amines) is only ∼5% of all *N*-relevant species within final cross-linked polymersomes (Figure S18d). This is also in agreement with zeta potential characterization results that H_2O_2-treated vesicles were barely charged (ca. +1.5 mV; Figure 2c).

In addition, oxidation-generated highly reactive quinone methide intermediates also possess several possible reaction pathways: (a) reaction with water; (b) single and double addition reactions with primary amines either released as small molecules or attached onto polymer scaffold via ester linkages, and the latter could be potentially released from the polymeric scaffold via amidation reactions with neighboring amine species; and (c) reaction with released small molecule pinacol (Scheme 3). To further explore this aspect, H_2O_2-incubated polymersome dispersion was diluted with methanol and filtered through a 0.22 μm syringe filter. The filtrate was then analyzed via the HPLC-MS technique (Figure S19). Main small molecule naphthalene-containing products include HMN (reaction product of quinone methide with water), HEAMN and $HEA(MN)_2$ (single and double addition adducts of quinone methide with HEA), and PinMN and $Pin(MN)_2$ (single and double addition adducts of quinone methide with pinacol). It is worth noting that the generation of small molecule HEAMN and $HEA(MN)_2$ also confirmed the occurrence of interchain and intrachain amidation reactions.

Quantitative analysis revealed that after H_2O_2 oxidation for 12 h, ∼19%, 1.9%, 43.6%, 7.9%, and 10.8% of NB moieties within the polymersome dispersion were released and transformed into small molecule HMN, HEAMN, $HEA(MN)_2$,

DOI: 10.1021/jacs.6b04115
J. Am. Chem. Soc. 2016, 138, 10452−10466

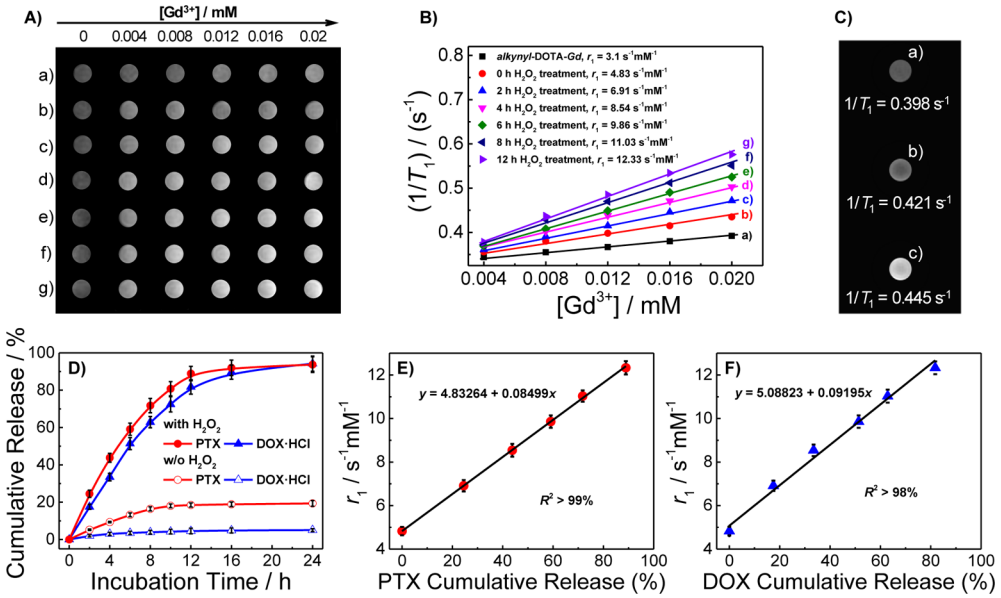

Figure 3. (A) T_1-weighted spin−echo MR images recorded for aqueous solutions of (a) small molecule *alkynyl*-DOTA-*Gd* complex and (b−g) *Gd*-**N8** polymersomes upon incubation with H_2O_2 (1 mM) for (b) 0 h, (c) 2 h, (d) 4 h, (e) 6 h, (f) 8 h, and (g) 12 h. (B) Gd^{3+} concentration-dependent water proton longitudinal relaxation rates ($1/T_1$) of (a) *alkynyl*-DOTA-*Gd* and (b−g) *Gd*-**N8** polymersome dispersion upon incubation with H_2O_2 (1 mM) for 0−12 h. (C) MR images recorded for (b) untreated control and (a,c) HeLa cells pretreated with (a) NAC (2.5 mM) and (c) PMA (200 nM) for 12 h at first and then incubated with CGKRK-decorated mixed vesicles coassembled from *Gd*-**N8** and *azide*-**N4** (9/1, wt/wt) for 12 h. (D) In vitro corelease profiles of hydrophobic PTX and hydrophilic DOX·HCl at 37 °C from PTX and DOX·HCl coloaded *Gd*-**N8** polymersomes (0.1 g/L; PBS buffer, pH 7.4, 10 mM) in the absence and presence of H_2O_2 (1 mM), respectively. (E,F) Linear correlation of cumulative release contents of (E) PTX and (F) DOX·HCl with corresponding r_1 relaxivity upon incubating *Gd*-**N8** polymersome dispersion with 1 mM H_2O_2 for specified time intervals. Data are presented as mean ± SD (n = 3).

PinMN, and Pin$(MN)_2$, respectively. We could further roughly estimate that ∼14.8% of total naphthyl moieties were retained within cross-linked polymersomes, resulting from addition reactions of quinone methide intermediates with amine-containing dangling side linkages, (i.e., generating secondary/tertiary amines). These dangling side linkages are conjugated to the polymeric backbone via ester linkages, which remain to be released from polymeric scaffold as small molecule products such as HEAMN and HEA$(MN)_2$ if neighboring primary/secondary amines are available (Scheme 3). Note that secondary amines generated on the scaffold might participate in further amidation reactions, contributing to vesicle cross-linking. Moreover, secondary/tertiary amine species could also partially remain in the protonated state, thus contributing to bilayer hydrophilicity and positive zeta potentials (Figure 2c). Therefore, upon H_2O_2 coincubation, the formation of extensive amide linkages along with residual protonated amines could lead to both cross-linking and bilayer hydrophobic-to-hydrophilic transition (Schemes 1 and 3).

Several issues are worthy of note in the above process. First, the apparent pK_a of primary amines will considerably decrease within initially hydrophobic vesicle bilayers. PAEMA homopolymer possesses a pK_a of ∼7.6, which is considerably lower than that of small molecule AEMA monomer (pK_a ≈ 8.8) due to that chain connectivity of the former resists the dense accumulation of cationic charges (i.e., being protonated).[28b] The decrease of effective pK_a of amine moieties in microenvironments with hydrophobic nature and/or high local concentration is not rare. Charge repression-induced pK_a shift was previously reported for thermoresponsive poly(*N*-isopropylacrylamide) containing ionizable comonomers,[29] the active pockets of folded proteins and enzymes,[30] and interior tertiary amines of PAMAM dendrimers.[31] In the latter two cases, pK_a shifts of ∼3−5 pH units could typically occur. The common feature is that charged moieties at high local densities resist building up of charges to offset charge repulsion. Thus, the effective decrease of apparent amine pK_a will favor intrachain and interchain amidation reactions (Scheme 3).

Second, within polymersome bilayers, NB capping moieties, caged amine functionalities, and ester linkages being subjected to amidation reactions are of high local concentration (∼1.0 mol/L[25c]). Thus, the high effective molarity and spatial proximity between oxidation-generated amines and ester linkages will greatly facilitate interchain amidation reactions, leading to extensive bilayer cross-linking. Finally, amidation reactions will further drive the protonation/deprotonation equilibrium of primary amines toward almost complete deprotonation, as amidation reactions selectively consume deprotonated amine species. It is worthy of note that the above-described oxidation-triggered bilayer cross-linking process is quite comparable to previously reported UV irradiation-induced "traceless" polymersome cross-linking and permeability switching.[18c] Closer examinations of relevant data revealed several noteworthy features. UV irradiation-induced vesicle cross-linking takes only ∼30 min, whereas H_2O_2-induced **N2** vesicle cross-linking in the current work takes ∼10−12 h. In the case of fast UV-triggered generation of primary amines, ∼10% of all *N*-relevant species exist as protonated amines for final cross-linked vesicles, with a zeta potential value of ca. +18 mV.[18c] However, for oxidation-induced vesicle cross-linking, the slow progress of the whole process rendered that only ∼5% of *N*-species exist as protonated primary amines for final cross-linked vesicles, with a final zeta potential of ca. +1.5 mV (Figure 2c and Figure S18d). Moreover, because UV light exhibits intrinsic limitations such as low penetration depth and possible damage toward biomolecules/living cells/tissues by long-term

DOI: 10.1021/jacs.6b04115
J. Am. Chem. Soc. 2016, 138, 10452−10466

irradiation, they are not applicable toward the construction of advanced biomedical functions such as smart drug nanocarriers, theranostic systems, and in vivo nanoreactors.

Experiments concerning **N2** vesicles physically encapsulating NR probes already revealed that during oxidation-triggered bilayer cross-linking, a hydrophobic-to-hydrophilic transition will occur simultaneously (Figure S13d). To further confirm that concurrent cross-linking and polarity switching have indeed occurred within vesicle bilayers upon H_2O_2 treating, we further examined polymersomes of *3HF*-**N5**, in which polarity-sensitive 3HF fluorophore was covalently conjugated onto the oxidation-responsive hydrophobic block.[32] Upon H_2O_2 treating of *3HF*-**N5** polymersome dispersion, continuous increase of ESICT band (excited-state intramolecular charge transfer; ∼440 nm) and concomitant decrease of ESIPT band (excited-state intramolecular proton transfer; ∼540 nm) intensities were observed (Figure 2e,f). These results indicated that within polymersome bilayers, the cross-linking process is synchronized with the transformation from hydrophobic bilayers to hydrophilic hydrogel-like membrane layers, which should then assist the release from and diffusion through of (bio)active molecules and substances across cross-linked bilayers (Scheme 1). Considering that H_2O_2 is an endogenous trigger associated with pathological sites, this new type of oxidation-responsive vesicles should act as excellent theranostic nanocarriers and switchable intracellular nanoreactors.

Engineering Oxidation-Responsive Polymeric Vesicles as Smart Theranostic Nanocarriers. Overproduction of H_2O_2 is associated with numerous diseases ranging from cancer and inflammatory diseases to neurodegenerative disorders. Therefore, the fabrication of H_2O_2-responsive theranostic nanovectors with integrated functions of targeted drug delivery and responsive MR imaging module is of great interest. Taking advantage of the synergistic microstructural reinforcement and bilayer permeability switching of oxidation-responsive polymersomes upon H_2O_2 treating (Scheme 1), we attempted to covalently conjugate MR imaging contrast agent, DOTA-*Gd* complex, onto the H_2O_2-responsive hydrophobic block. Upon self-assembling into vesicular aggregates, DOTA-*Gd* moieties were initially located within hydrophobic bilayers, and the rate of exchange with surrounding water molecules was considerably hampered, exhibiting relatively low T_1 relaxivity (r_1).[21,33] In contrast, subsequent H_2O_2-actuated bilayer cross-linking and permeabilizing will then render the Gd complex to locate within hydrophilic milieu, which is expected to prominently enhance r_1. Because the bilayer permeabilization process will concomitantly lead to the release of both hydrophobic and hydrophilic payloads (Scheme 1), we also speculate that the drug release profile might be closely correlated with time-dependent changes in MR imaging signals.

Toward this end, we synthesized amphiphilic BCP covalently conjugated with MR imaging contrast agent, *Gd*-**N8** (Scheme S2b), which self-assembled into polymersomes in aqueous media (Figure S1f). Upon coincubating with 1 mM H_2O_2 for varying time periods, typical T_1-weighted spin−echo MR images recorded for aqueous dispersions of *Gd*-**N8** polymersomes with varying Gd^{3+} levels are shown in Figure 3A. Generally, MR imaging signals of *Gd*-**N8** polymersome dispersions increased with both Gd^{3+} concentrations and H_2O_2 incubation duration. For instance, the initial r_1 value of *Gd*-**N8** vesicle dispersion was ∼4.83 s^{-1} mM^{-1}, whereas it increased to ∼6.91, 8.54, 9.86, 11.03, and 12.33 s^{-1} mM^{-1} after 2, 4, 6, 8, and 12 h treating with 1 mM H_2O_2, respectively (Figure 3B). Note that the r_1 value of small molecule *alkynyl*-DOTA-*Gd* complex was ∼3.1 s^{-1} mM^{-1}. The elevated r_1 of *Gd*-**N8** polymersome dispersion triggered by H_2O_2 should be ascribed to two cooperative effects: (i) conjugation of DOTA-*Gd* onto the responsive block and subsequent self-assembly significantly decreased tumbling and rotational rates of contrast agents, which was evidenced by the slightly increased r_1 value of *Gd*-**N8** polymersome dispersion without H_2O_2 treating; and (ii) H_2O_2-triggered permeabilization of *Gd*-**N8** vesicle bilayers rendered the surrounding milieu of DOTA-*Gd* complex to be hydrophilic, and vesicle cross-linking could covalently bind Gd complex within bilayer membranes.

During *Gd*-**N8** vesicle formation, both hydrophobic paclitaxel (PTX) and hydrophilic doxorubicin hydrochloride (DOX·HCl) anticancer drugs could be coloaded into bilayers and aqueous lumens (Figure S20), respectively. Along with increased T_1 relaxivity upon treating with 1 mM H_2O_2 (Figure 3B), ∼94% DOX and ∼93% PTX were released within ∼24 h coincubation duration, whereas only ∼5% DOX and ∼19% PTX were released within the same time period in the absence of H_2O_2 (Figure 3D). More intriguingly, a linear correlation between cumulative PTX/DOX release extents and T_1 relaxivities could be obtained (Figure 3E,F). The above results indicated that MR imaging could serve as a noninvasive technique to in situ monitor the oxidation-triggered drug release process from *Gd*-**N8** polymersomes. In addition, considering the overproduction of ROS such as H_2O_2 at inflammatory sites, as a proof-of-concept example, H_2O_2-regulated release of anti-inflammatory dexamethasone (DEX) drug from **N2** polymersomes was also examined at varying H_2O_2 concentrations (Figure S21). These results revealed that H_2O_2-responsive vesicles could serve as smart delivery nanocarriers for both anticancer drugs and anti-inflammatory drugs.

Given that cellular ROS species are primarily produced within mitochondria, we further decorated the surface of oxidation-responsive polymersomes with mitochondria-targeting CGKRK peptide[23] via double "click" chemistry (Figure S22). Briefly, **N2** and azide-terminated *azide*-**N4** BCPs (9/1, wt/wt) coassembled into polymersomes at first. This was followed by consecutive copper-free "click" chemistry and thiol-maleimide addition reactions, yielding CGKRK peptide-decorated polymersomes (Figure S22a). Although the $\langle D_h \rangle$ did not exhibit any appreciable changes after peptide conjugation (Figure S22b), a considerable increase of zeta potential value from ca. −20 to ca. −3 mV was observed (Figure S22c).

Cellular uptake of CGKRK-decorated mixed vesicles coassembled from **N2**, *azide*-**N4**, and *FMA*-**N7** (6/1/3, weight ratios) was then examined against HeLa cells by confocal laser scanning microscopy (CLSM), using CGKRK-blank mixed vesicles as a control. The uptake of oxidation-responsive polymersomes was tracked by green-emitting FMA moieties and quantified by the evolution of green channel emission intensities (Figure S23). Upon coculture with CGKRK-free mixed vesicles for 12 h, only weak green channel emission was detected within cells, and the colocalization ratio between FITC green channel emission of vesicles and red channel emission of mitochondria-staining MitoTracker Red was ∼20% (Figure S23a,d,e). In contrast, upon coculture with CGKRK-decorated mixed vesicles for 4 h, increased cellular internalization was discerned. Further increase of both intensities and colocalization ratios between green channel emission of FITC-vesicles and red channel emission of MitoTracker Red was

DOI: 10.1021/jacs.6b04115
J. Am. Chem. Soc. 2016, 138, 10452−10466

achieved upon extending the coculture duration to 12 h (Figure S23b–e). However, the overall mitochondria-targeting performance (~35% colocalization ratio after 12 h incubation) of polymersomes is quite compromised due to their large size (~500 nm). Previous literature reports indicated that nanoparticles with size dimensions exceeding 200 nm would hardly target into cellular mitochondria.[34] To explore the role of polymersome size on mitochondria-targeting efficiency, smaller-sized polymersomes with $\langle D_h \rangle$ of ~120 nm were fabricated via membrane extrusion technique (see Figure S24 for details).[35] The mitochondria-targeting efficiency was then evaluated (Figure S25). The results revealed that CGKRK peptide-decorated small-sized polymersomes exhibit prominently improved mitochondria-targeting performance as compared to both nontargeting small-sized vesicles and mitochondria-targeting large-sized vesicles (Figure S25e).

We further explored whether CGKRK-decorated mixed vesicles coassembled from *Gd*-**N8** and *azide*-**N4** BCPs (9/1, wt/wt) could achieve oxidation-triggered synergistic MR contrast enhancement and drug release at cellular levels. Untreated HeLa cells, HeLa cells treated with *N*-acetyl-*L*-cysteine (NAC; 2.5 mM) as a ROS scavenger, and HeLa cells treated with phorbol-12-myristate-13-acetate (PMA; 200 nM) as an intracellular ROS stimulator were then coincubated with CGKRK-decorated *Gd*-**N8** mixed vesicles. The untreated control exhibited a spin–lattice relaxation rate, $1/T_1$, of ~0.421 s^{-1} (Figure 3C, middle), and NAC-pretreated HeLa cells possessed $1/T_1$ value of ~0.398 s^{-1} (Figure 3C, top). On the other hand, PMA-pretreated HeLa cells exhibited prominently enhanced MR imaging contrast ($1/T_1$ = 0.445 s^{-1}; Figure 3C, bottom). The above results suggested that oxidation-responsive polymersomes could act as milieu-responsive MR imaging contrast agents and report the magnitude of intracellular oxidative stress in a noninvasive manner.

Apart from oxidative milieu-triggered MR imaging contrast enhancement, we deduced that controlled drug release module could also be achieved under cellular conditions by taking advantage of H_2O_2-mediated concurrent bilayer cross-linking and permeability switching. We then assessed the controlled release behavior of **N2** polymersomes within RAW264.7 macrophages using a model drug, fluorescein diacetate (FDA). FDA is initially nonfluorescent but highly emissive after cleavage of the two ester linkages. Interestingly, after pretreating RAW264.7 macrophages with PMA (200 nM) for 12 h, FDA-loaded **N2** polymersomes exhibited more intense emission than FDA-loaded H_2O_2-inert PEO-*b*-polystyrene (PEO_{45}-*b*-PS_{88}) vesicles (Figures S26 and S27).[25e] This should be ascribed to the H_2O_2-actuated hydrophobic-to-hydrophilic transition of **N2** polymersome bilayers and triggered release of encapsulated FDA payload from polymersomes into the cytoplasm, followed by esterase-triggered cleavage of ester linkages of FDA. However, this process was substantially prohibited for H_2O_2-inert PEO-*b*-PS vesicles due to the inherently impermeable nature of vesicle bilayers.

Next, we further examined cytotoxicities of blank and drug-loaded oxidation-responsive polymersomes. CGKRK-decorated **N2** polymersome dispersions with a concentration up to ~1.0 g/L exhibited negligible cytotoxicity against both HeLa cells and RAW264.7 macrophages (Figure S28). However, ~74% PMA-pretreated HeLa cells were killed after 48 h coculture with PTX and DOX·HCl coloaded CGKRK-decorated **N2** vesicles (Figure S29). Note that PMA alone and PMA@vesicles are noncytotoxic toward HeLa cells. Additional live/dead assays also agreed well with MTT assay results. Negligible cell death could be discerned for blank vesicles, whereas much lower cell survival rate was recorded in the presence of PTX/DOX@ vesicles (Figure S30a,b). Moreover, when HeLa cells were pretreated with NAC (2.5 mM) for 12 h, the cytotoxicity of drug coloaded vesicles dramatically decreased; nonetheless, pretreatment with 200 nM PMA could considerably enhance cytotoxicities (Figure S30c,d).

CLSM technique was then utilized to quantitatively interrogate intracellular drug release from PTX/DOX@vesicles (Figure S31a–c). After 24 h coincubation, red channel emission intensities of DOX, which was released from **N2** polymersomes, within cell nuclei and colocalization ratios between blue channel emission of cell nuclei-staining DAPI (4′,6-diamidino-2-phenylindole) and red channel emission of DOX were dramatically affected by cellular H_2O_2 levels (Figure S31d,e). Specifically, the colocalization ratio dropped from ~54% for the untreated control to ~18% for NAC-pretreated cells, and increased to ~87% for PMA-pretreated cells (Figure S31e). These results implied the crucial role of cellular H_2O_2 concentrations in mediating the drug release profile of oxidation-responsive polymersomes (Figure 3D). Overall, oxidation-responsive polymersomes exhibiting intracellular H_2O_2-triggered synchronized bilayer cross-linking and permeabilization could be utilized to construct smart theranostic nanocarriers, with the drug release process in situ noninvasively monitored by changes in MR imaging signals.

Insights into Synchronized Bilayer Cross-Linking and Permeability Switching of Oxidation-Triggered Polymersomes within Live Cells and Construction of Intracellular Nanoreactors. Triggered assembly and disassembly by taking advantage of endogenous stimuli have been extensively explored previously;[36] however, to the best of our knowledge, intracellular milieu-triggered cross-linking of BCP polymersomes associated with membrane permeability switching inside live cells has not been achieved yet. In previous sections, we established that arylboronate-containing oxidation-responsive vesicles could undergo H_2O_2-mediated bilayer cross-linking and concurrent membrane hydrophobic-to-hydrophilic transition (Figures 2 and 3; Scheme 1); this feature was further utilized to design smart theranostic nanocarriers exhibiting a linear correlation between drug release contents and MR signal intensities. Under cellular conditions, intracellular H_2O_2 levels, altered via PMA or NAC addition, could also modulate MR signal intensities (Figure 3C) and drug release profiles of oxidation-responsive polymersomes conjugated with DOTA-*Gd* complex (Figure 3C, Figures S27–S31) . However, the following issues remain to be elucidated: (i) Will concurrent bilayer cross-linking and permeabilization of oxidation-responsive vesicles occur inside live cells? (ii) Could the above process be triggered by intracellular endogenous oxidative milieu? (iii) Could oxidation-responsive polymersomes maintain structural integrity and function as stable intracellular nanoreactors? As **N2** polymersomes possess size dimensions of ~500 nm (Figure 2a), direct in situ microstructural characterization toward the details of bilayer cross-linking/permeability tuning under intracellular milieu is quite challenging. In the following section, we attempted to probe the structural integrity and evolution of bilayer permeability via indirect approaches. On the basis of further verified intracellular milieu-triggered vesicle cross-linking and permeabilization, we

DOI: 10.1021/jacs.6b04115
J. Am. Chem. Soc. 2016, 138, 10452–10466

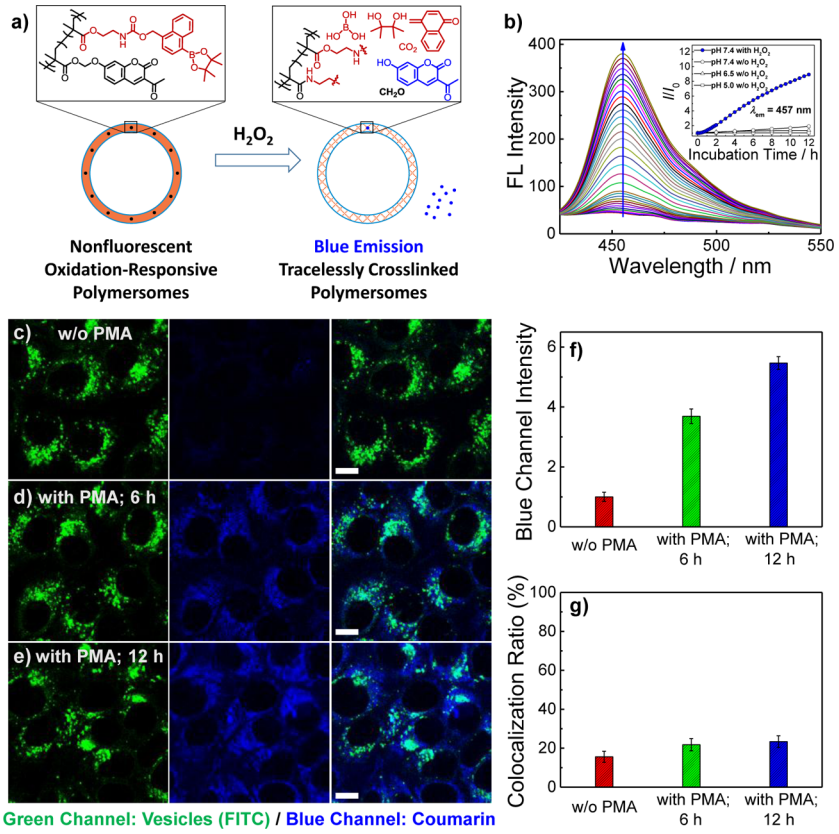

Figure 4. (a) Schematics of intracellular H_2O_2-triggered generation of primary amines, followed by fluorogenic amidation reactions and amidation-incurred cross-linking of *CM*-N6 polymersome bilayers containing covalently conjugated acyloxymethyl ether-caged coumarin fluorophores. (b) Evolution of fluorescence emission spectra (λ_{ex} = 405 nm) of *CM*-**N6** polymersome dispersion (0.1 g/L) upon treatment with H_2O_2 (1 mM; PBS buffer, pH 7.4, 10 mM; 25 °C). The inset in (b) shows time-dependent changes in normalized emission intensities at 457 nm when the polymersome dispersion was incubated at pH 5.0, pH 6.5, and pH 7.4 in the absence of H_2O_2. (c–e) Representative green channel (FITC-vesicles, 520 ± 20 nm) and blue channel (coumarin, 450 ± 20 nm) CLSM images (scale bar: 10 μm) recorded for HeLa cells upon (d) 2 h and (c,e) 8 h additional incubation after 4 h coculture with CGKRK-decorated mixed vesicles coassembled from *CM*-**N6**, *azide*-**N4**, and *FMA*-**N7** (6/1/3, weight ratios); note that cells were pretreated (c) without PMA or (d,e) with PMA (200 nM) for 12 h. (f) Normalized blue channel (coumarin moieties) emission intensities and (g) colocalization ratio analysis between green channel (FITC-vesicles) and blue channel (coumarin moieties) images quantified from CLSM results (c–e). Data are presented as mean ± SD (n = 3).

constructed intracellular nanoreactors toward the fluorogenic detection of cytoplasmic thiol-containing compounds.

We started to probe that after internalization of oxidation-responsive polymersomes, cellular H_2O_2-triggered generation of primary amines and subsequent amidation reactions within vesicle bilayers could indeed occur (Scheme 3). Toward this goal, fluorogenic methacrylate monomer, CMA, containing caged 7-hydroxycoumarin was synthesized and copolymerized into the oxidation-responsive hydrophobic PNBMA block (*CM*-**N6**; Figure 4a, Schemes S1 and S2a). For the vesicle dispersion self-assembled from *CM*-**N6**, primary amines newly generated by H_2O_2 oxidation will undergo amidation reactions with ester linkages. This process will also trigger the release of highly fluorescent 7-hydroxycoumarin derivative via the aminolysis of ester linkage (amidation) in CMA monomer. Prior to the evaluation of triggered release of 7-hydroxycoumarin derivative from *CM*-**N6** polymersomes, the reactivity of CMA monomer toward H_2O_2 (1 mM) and stability of *CM*-**N6** polymersomes under different pH conditions (i.e., pH 5.0, 6.5, and 7.4) were examined to ensure that fluorescence emission turn-on is solely due to amidation-triggered release of 7-hydroxycoumarin derivative. It was observed that CMA monomer is quite stable either in the absence or in the presence of H_2O_2 (Figure S32). In addition, *CM*-**N6** polymersomes are also stable under slightly acidic (pH 5.0 and pH 6.5; comparable to acidic intracellular organelles) or neutral pH conditions in the absence of H_2O_2 (Figure 4b). However, upon treating *CM*-**N6** polymersomes with 1 mM H_2O_2, fluorescence emission exhibited an ~9-fold increase after 12 h (Figure 4b), suggesting that extensive amidation reactions could indeed occur within hydrophobic vesicle bilayers. H_2O_2-induced emission turn-on of coumarin moieties within *CM*-**N6** vesicles was further visualized inside HeLa cells. For CGKRK-decorated mixed vesicles coassembled from *CM*-**N6**, *azide*-**N4**, and *FMA*-**N7** (6/1/3, weight ratios), CLSM images revealed a gradual increase of blue channel emission (corresponding to released coumarin derivative) intensities with coincubation time for PMA-pretreated HeLa cells, whereas negligible blue emission was detected for the untreated control (Figure 4c–e; for lower magnification images, see Figure S33). Quantitative analysis revealed that blue channel emission intensities increased ~3.7-fold (6 h incubation) and ~5.5-fold (12 h incubation) for PMA-pretreated HeLa cells, respectively, as compared to untreated HeLa cells (Figure 4f). In addition, colocalization ratios between blue channel emission of newly generated 7-hydroxycoumarin and green channel emission of FMA-labeled mixed vesicles remained constantly low (<24%), which was irrespective of PMA pretreatment or not. This further

DOI: 10.1021/jacs.6b04115
J. Am. Chem. Soc. 2016, 138, 10452–10466

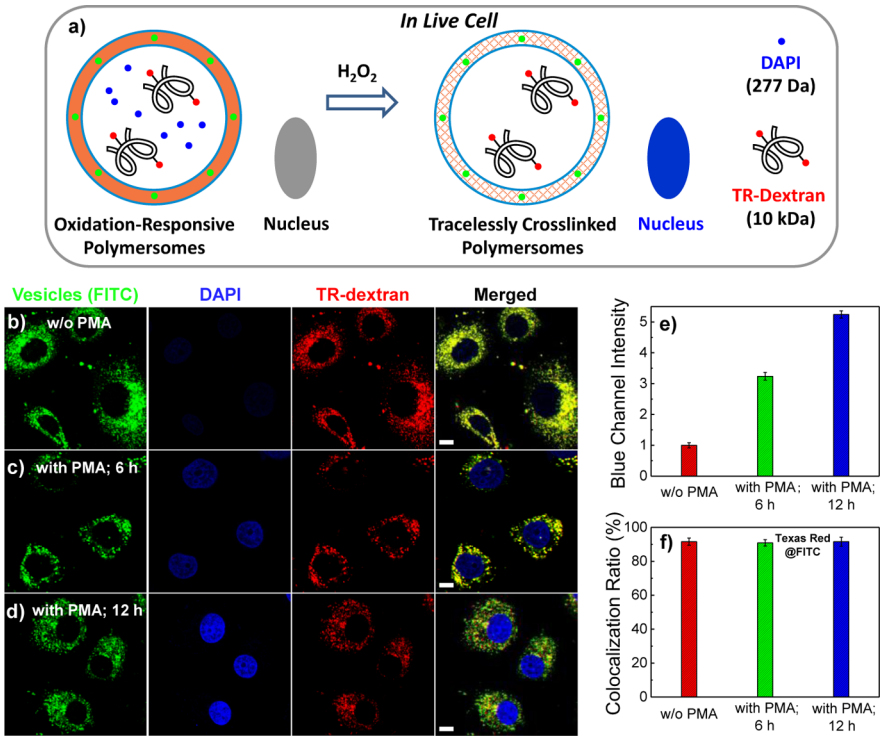

Figure 5. (a) Schematics of intracellular H_2O_2-triggered traceless cross-linking and permeability switching of bilayer membranes of polymersomes coloaded with nucleus-staining small molecule DAPI dye and Texas Red-dextran (TR-dextran, MW ≈ 10 kDa). Intracellular oxidation triggers DAPI release from polymersomes due to concurrent bilayer cross-linking and hydrophobic-to-hydrophilic transition, whereas TR-dextran was retained within the vesicle interior due to its large size dimension. (b–d) Representative green channel (FITC-vesicles), blue channel (DAPI), and red channel (TR-dextran) CLSM images (scale bar: 10 μm) recorded for HeLa cells upon (c) 2 h and (b,d) 8 h additional incubation after 4 h coculture with CGKRK-decorated mixed vesicles coassembled from **N2**, *azide*-**N4**, and *FMA*-**N7** (6/1/3, weight ratios) coloaded with DAPI and TR-dextran; note that cells were untreated (b) or pretreated with PMA (c,d) for 12 h. (e) Normalized blue channel (DAPI) emission intensities and (f) colocalization ratio analysis between red channel (TR-dextran) and green channel (FITC-vesicles) images quantified from CLSM results (b–d). Error bars show mean ± SD (n = 3).

confirmed the release of 7-hydroxycoumarin derivative from polymersome bilayers due to amidation reactions (Scheme 3).

Next, we attempted to indirectly visualize H_2O_2-triggered cross-linking of bilayer membranes and synergistic permeability switching. Specifically, hydrophilic cell nuclei-staining small molecule DAPI dye (MW = 277 Da) and Texas Red-dextran (TR-dextran, MW ≈ 10 kDa) were coencapsulated into the aqueous lumen of CGKRK-decorated mixed vesicles coassembled from **N2**, *azide*-**N4**, and *FMA*-**N7** (6/1/3, weight ratios) to probe permeability changes and polymersome integrity upon oxidation under cellular conditions (Figure 5 and Figure S34a–c).

The general design is that oxidation-actuated bilayer permeability changes will trigger the release of small molecule hydrophilic DAPI, which will then spontaneously diffuse into and stain cell nuclei. On the other hand, if microstructural integrity of vesicles could be maintained via concomitant bilayer cross-linking, TR-dextran (MW ≈ 10 kDa) is expected to be retained within vesicle interiors due to its large size dimensions as compared to DAPI (Figure 5a). CLSM images (Figure 5b–d) showed that for PMA-pretreated HeLa cells, blue-emitting DAPI diffused from vesicular interiors, and most of them were intercalated into DNA double strands within cell nuclei and rendered highly fluorescent. Blue channel emission intensities exhibited an ∼3.2-fold increase after 6 h coincubation and an ∼5.2-fold increase after 12 h coincubation for PMA-pretreated HeLa cells, respectively, as compared to the untreated control (Figure 5e). These results were in agreement with H_2O_2-triggered release of FDA and DOX·HCl from oxidation-responsive vesicles under simulated oxidative conditions (Figures S27 and S31). Despite cellular oxidative milieu-triggered permeability switching of bilayer membranes, it was found that encapsulated TR-dextran with much higher MW (dextran ∼10 kDa vs DAPI ∼277 Da and DOX ∼543 Da) cannot be released from polymersomes (Figure S34d). Moreover, colocalization ratios between red channel emission of TR-dextran and green channel emission of FMA-labeled vesicles, as quantified from CLSM measurements, remained constantly high (>90%; Figure 5f). The above results thus clearly confirmed that under cellular conditions, the oxidative milieu could trigger concomitant bilayer cross-linking and membrane permeability switching of oxidation-responsive vesicles (Scheme 1).

The feature of intracellular milieu-triggered vesicle cross-linking and bilayer permeabilizing could allow for the construction of sustained release nanocontainers and long-term stable in vivo nanoreactors for in situ production of antibiotics, therapeutic drugs, and diagnostic agents. Under these application circumstances, switchable and selective transport of internal and external substances through vesicular nanoreactor membranes is a prerequisite. As a proof-of-example, we encapsulated fluorogenic CM-dextran (MW ≈ 10 kDa), which are reactive toward (cytosolic) thiol-containing bioactive molecules (e.g., GSH and cysteine, Cys), into the aqueous interior of polymersomes. Before H_2O_2 oxidation, external GSH or Cys cannot diffuse though hydrophobic

DOI: 10.1021/jacs.6b04115
J. Am. Chem. Soc. 2016, 138, 10452–10466

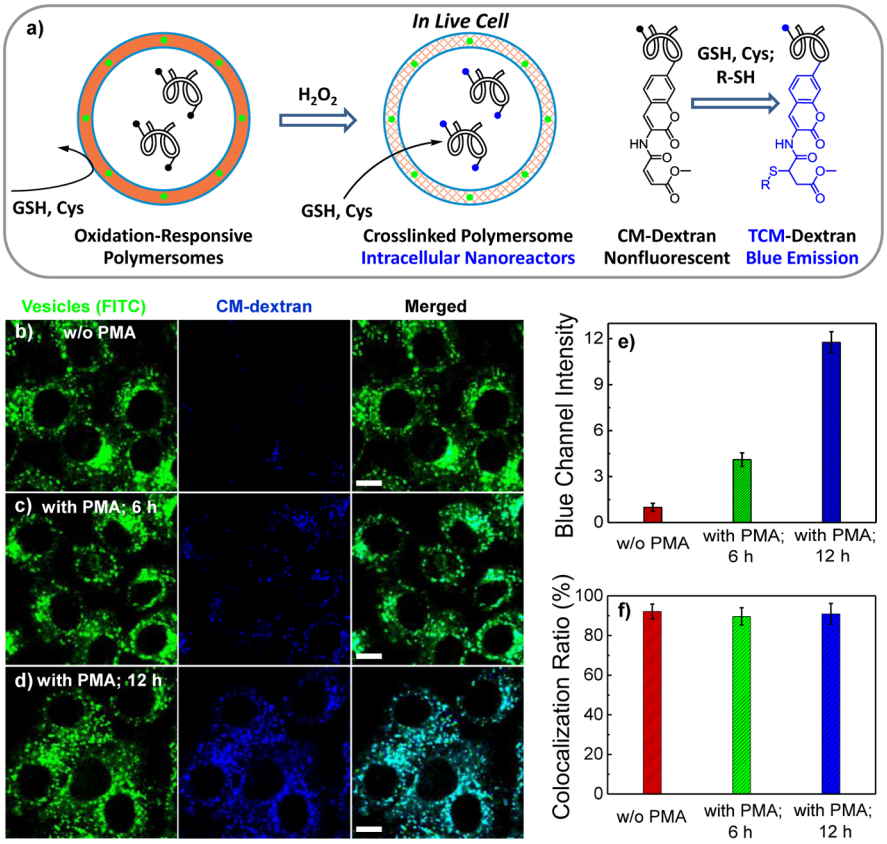

Figure 6. (a) Schematics of the construction of intracellular nanoreactors based on oxidation-responsive polymersomes encapsulating water-soluble and thiol-reactive fluorogenic CM-dextran (MW ≈ 10 kDa). Intracellular H_2O_2 triggered cross-linking and permeability switching of bilayer membranes allows for controlled diffusion of cytosolic thiol-containing bioactive molecules (e.g., GSH, Cys) into the aqueous interior and leads to fluorescence emission turn-on. (b–d) Representative green channel (FITC-vesicles) and blue channel (CM-dextran) CLSM images (scale bar: 10 μm) recorded for HeLa cells upon (c) 2 h and (b,d) 8 h additional incubation after 4 h coculture with CGKRK-decorated mixed vesicles coassembled from **N2**, *azide*-**N4**, and *FMA*-**N7** (6/1/3, weight ratios) loaded with CM-dextran; note that cells were pretreated (b) without PMA or (c,d) with PMA for 12 h. (e) Normalized blue channel (CM-dextran) emission intensities and (f) colocalization ratio analysis between blue channel and green channel (FITC-vesicles) images quantified from CLSM results (b–d). Data are expressed as means ± SD (n = 3).

bilayers and undergo fluorogenic Michael addition reactions with encapsulated CM-dextran; whereas upon H_2O_2-triggered bilayer permeability switching and vesicle cross-linking, CM-dextran will be rendered highly fluorescent due to the accessibility of GSH and Cys molecules (Figure 6a). CM-dextran was then synthesized (Figure S35a), and its fluorogenic nature toward thiol-containing compounds (e.g., GSH) was verified, exhibiting a cumulative ∼30-fold emission increase within ∼30 min (Figure S35). However, after encapsulating CM-dextran into **N2** polymersomes without H_2O_2 pretreatment, we cannot observe any discernible emission enhancement within the same incubation period upon GSH addition (Figure S36). This could be ascribed to the low permeability of GSH through untreated hydrophobic **N2** bilayers. In sharp contrast, a prominent emission increase was observed for H_2O_2-pretreated **N2** polymersomes encapsulating CM-dextran upon GSH addition, confirming that H_2O_2 treatment resulted in bilayer permeability switching (Figure S36b).

We further attempted to construct intracellular nanoreactors toward cytoplasmic thiol-containing biomolecules, with the nanoreactor activity tunable by cellular oxidative stresses. CGKRK-decorated mixed vesicles coassembled from **N2**, *azide*-**N4**, and *FMA*-**N7** (6/1/3, weight ratios) were loaded with fluorogenic CM-dextran. As speculated, the vesicular nanoreactor could be activated by utilizing cellular H_2O_2 as the fuel. Upon coincubation with PMA-pretreated HeLa cells, the intensity of blue channel emission corresponding to fluorescent CM-GSH adducts exhibited ∼4.1-fold (6 h incubation) and ∼11.8-fold (12 h incubation) increases, as compared to untreated HeLa cells (Figure 6b–e; for lower magnification images, see Figure S37). Moreover, the blue channel emission of reacted CM-dextran and green channel emission of FMA-labeled polymersomes showed a high extent of colocalization (i.e., colocalization ratio >89%) throughout the whole incubation duration (Figure 6f). The above results indicated that intracellular oxidative milieu could be further exploited to construct switchable in vivo nanoreactors on the basis of oxidation-responsive polymersomes.

■ CONCLUSIONS

In summary, four types of H_2O_2-responsive monomers containing varying arylboronate capping moieties and self-immolative linkages were synthesized. The corresponding amphiphilic BCPs could self-assemble in aqueous media into diverse aggregates including spherical nanoparticles, polymersomes, and large compound vesicles possessing varying H_2O_2 response kinetics and distinct microstructural transformation features. For oxidation-responsive polymersomes, coincubation with H_2O_2 under simulated biological conditions (∼1 mM H_2O_2) or under cellular oxidative milieu inside live cells led to

DOI: 10.1021/jacs.6b04115
J. Am. Chem. Soc. 2016, 138, 10452–10466

cleavage of arylboronate capping moieties at first, followed by cascade decaging reactions and generation of primary amine moieties. The latter further resulted in vesicle cross-linking and concomitant permeabilization of bilayer membranes. Toward the construction of smart theranostic nanocarriers, oxidation-responsive vesicles were utilized to achieve targeted delivery and sustained release of both hydrophilic and hydrophobic payloads modulated by cellular oxidation stress, and this process could be noninvasively monitored by MR imaging signal intensity changes in real-time. We further demonstrate that H_2O_2-responsive polymersomes could be tailored as long-term stable intracellular nanoreactors benefiting from H_2O_2-activatable selective transport of specific substances (e.g., cytoplasmic GSH and Cys) into aqueous interiors. Overall, this work opens a new avenue toward the fabrication of smart nanocarriers and nanoreactors with long-acting performance inside live cells or even under in vivo conditions, by taking advantage of biologically relevant endogenous triggering stimuli.

■ ASSOCIATED CONTENT

Supporting Information

The Supporting Information is available free of charge on the ACS Publications website at DOI: 10.1021/jacs.6b04115.

Full experimental details, NMR, ESI−MS, FT-IR, UV/vis, XPS, fluorescence spectra, DLS, additional TEM and CLSM images, and control experiments (PDF)

■ AUTHOR INFORMATION

Corresponding Author

*sliu@ustc.edu.cn

Notes

The authors declare no competing financial interest.

■ ACKNOWLEDGMENTS

Financial support from the National Natural Science Foundation of China (NNSFC) projects (21504087, 21274137, 51273190, 51473153, and 51033005), Fundamental Research Funds for Central Universities, and Anhui Provincial Natural Science Foundation projects (1308085MH166 and 1508085ME98) is gratefully acknowledged.

■ REFERENCES

(1) Winterbourn, C. C. *Nat. Chem. Biol.* **2008**, *4*, 278−286.

(2) Trachootham, D.; Alexandre, J.; Huang, P. *Nat. Rev. Drug Discovery* **2009**, *8*, 579−591.

(3) Szatrowski, T. P.; Nathan, C. F. *Cancer Res.* **1991**, *51*, 794−798.

(4) Johansson, A.; Jesaitis, A. J.; Lundqvist, H.; Magnusson, K. E.; Sjolin, C.; Karlsson, A.; Dahlgren, C. *Cell. Immunol.* **1995**, *161*, 61−71.

(5) Bandyopadhyay, A.; Gao, J. *J. Am. Chem. Soc.* **2016**, *138*, 2098−2101.

(6) Savina, A.; Peres, A.; Cebrian, I.; Carmo, N.; Moita, C.; Hacohen, N.; Moita, L. F.; Amigorena, S. *Immunity* **2009**, *30*, 544−555.

(7) (a) Noh, J.; Kwon, B.; Han, E.; Park, M.; Yang, W.; Cho, W.; Yoo, W.; Khang, G.; Lee, D. *Nat. Commun.* **2015**, *6*, 6907−6915. (b) Wilson, D. S.; Dalmasso, G.; Wang, L. X.; Sitaraman, S. V.; Merlin, D.; Murthy, N. *Nat. Mater.* **2010**, *9*, 923−928.

(8) Zhang, L. F.; Eisenberg, A. *Science* **1995**, *268*, 1728−1731.

(9) (a) Bachelder, E. M.; Beaudette, T. T.; Broaders, K. E.; Dashe, J.; Frechet, J. M. J. *J. Am. Chem. Soc.* **2008**, *130*, 10494−10495. (b) Onaca, O.; Enea, R.; Hughes, D. W.; Meier, W. *Macromol. Biosci.* **2009**, *9*, 129−139. (c) Cui, L. N.; Cohen, J. L.; Chu, C. K.; Wich, P. R.; Kierstead, P. H.; Frechet, J. M. J. *J. Am. Chem. Soc.* **2012**, *134*, 15840−15848.

(10) Graff, A.; Sauer, M.; Van Gelder, P.; Meier, W. *Proc. Natl. Acad. Sci. U. S. A.* **2002**, *99*, 5064−5068.

(11) Discher, D. E.; Ortiz, V.; Srinivas, G.; Klein, M. L.; Kim, Y.; David, C. A.; Cai, S. S.; Photos, P.; Ahmed, F. *Prog. Polym. Sci.* **2007**, *32*, 838−857.

(12) Marguet, M.; Bonduelle, C.; Lecommandoux, S. *Chem. Soc. Rev.* **2013**, *42*, 512−529.

(13) (a) Wilson, D. A.; Nolte, R. J. M.; van Hest, J. C. M. *Nat. Chem.* **2012**, *4*, 268−274. (b) Langowska, K.; Palivan, C. G.; Meier, W. *Chem. Commun.* **2013**, *49*, 128−130.

(14) (a) Broaders, K. E.; Grandhe, S.; Frechet, J. M. *J. Am. Chem. Soc.* **2011**, *133*, 756−758. (b) Ma, N.; Li, Y.; Ren, H. F.; Xu, H. P.; Li, Z. B.; Zhang, X. *Polym. Chem.* **2010**, *1*, 1609. (c) Ma, N.; Li, Y.; Xu, H. P.; Wang, Z. Q.; Zhang, X. *J. Am. Chem. Soc.* **2010**, *132*, 442−443. (d) de Gracia Lux, C.; Joshi-Barr, S.; Nguyen, T.; Mahmoud, E.; Schopf, E.; Fomina, N.; Almutairi, A. *J. Am. Chem. Soc.* **2012**, *134*, 15758−15764. (e) Gupta, M. K.; Meyer, T. A.; Nelson, C. E.; Duvall, C. L. *J. Controlled Release* **2012**, *162*, 591−598. (f) Song, C.-C.; Ji, R.; Du, F.-S.; Liang, D.-H.; Li, Z.-C. *ACS Macro Lett.* **2013**, *2*, 273−277. (g) Wang, J.; Sun, X.; Mao, W.; Sun, W.; Tang, J.; Sui, M.; Shen, Y.; Gu, Z. *Adv. Mater.* **2013**, *25*, 3670−3676. (h) Xu, H. P.; Cao, W.; Zhang, X. *Acc. Chem. Res.* **2013**, *46*, 1647−1658. (i) Cao, W.; Gu, Y.; Li, T.; Xu, H. *Chem. Commun.* **2015**, *51*, 7069−7071. (j) Kang, Y.; Ma, Y.; Zhang, S.; Ding, L.-S.; Li, B.-J. *ACS Macro Lett.* **2015**, *4*, 543−547.

(15) (a) Napoli, A.; Boerakker, M. J.; Tirelli, N.; Nolte, R. J. M.; Sommerdijk, N. A. J. M.; Hubbell, J. A. *Langmuir* **2004**, *20*, 3487−3491. (b) Napoli, A.; Valentini, M.; Tirelli, N.; Muller, M.; Hubbell, J. A. *Nat. Mater.* **2004**, *3*, 183−189. (c) Scott, E. A.; Stano, A.; Gillard, M.; Maio-Liu, A. C.; Swartz, M. A.; Hubbell, J. A. *Biomaterials* **2012**, *33*, 6211−6219. (d) Liu, L. C.; Rui, L. L.; Gao, Y.; Zhang, W. A. *Polym. Chem.* **2015**, *6*, 1817−1829.

(16) (a) Sauer, M.; Haefele, T.; Graff, A.; Nardin, C.; Meier, W. *Chem. Commun.* **2001**, 2452−2453. (b) Discher, D. E.; Eisenberg, A. *Science* **2002**, *297*, 967−973.

(17) (a) Thurmond, K. B.; Kowalewski, T.; Wooley, K. L. *J. Am. Chem. Soc.* **1996**, *118*, 7239−7240. (b) Discher, B. M.; Bermudez, H.; Hammer, D. A.; Discher, D. E.; Won, Y. Y.; Bates, F. S. *J. Phys. Chem. B* **2002**, *106*, 2848−2854. (c) O'Reilly, R. K.; Hawker, C. J.; Wooley, K. L. *Chem. Soc. Rev.* **2006**, *35*, 1068−1083.

(18) (a) Gaitzsch, J.; Appelhans, D.; Grafe, D.; Schwille, P.; Voit, B. *Chem. Commun.* **2011**, *47*, 3466−3468. (b) Gaitzsch, J.; Appelhans, D.; Grafe, D.; Schwille, P.; Voit, B. *Angew. Chem., Int. Ed.* **2012**, *51*, 4448−4451. (c) Wang, X.; Liu, G.; Hu, J.; Zhang, G.; Liu, S. *Angew. Chem., Int. Ed.* **2014**, *53*, 3138−3142.

(19) (a) Chang, M. C. Y.; Pralle, A.; Isacoff, E. Y.; Chang, C. J. *J. Am. Chem. Soc.* **2004**, *126*, 15392−15393. (b) Lippert, A. R.; De Bittner, G. C. V.; Chang, C. J. *Acc. Chem. Res.* **2011**, *44*, 793−804.

(20) Kim, E. J.; Bhuniya, S.; Lee, H.; Kim, H. M.; Cheong, C.; Maiti, S.; Hong, K. S.; Kim, J. S. *J. Am. Chem. Soc.* **2014**, *136*, 13888−13894.

(21) Viger, M. L.; Sankaranarayanan, J.; de Gracia Lux, C.; Chan, M.; Almutairi, A. *J. Am. Chem. Soc.* **2013**, *135*, 7847−7850.

(22) (a) Li, C. H.; Hu, J. M.; Liu, T.; Liu, S. Y. *Macromolecules* **2011**, *44*, 429−431. (b) Li, C.; Wu, T.; Hong, C.; Zhang, G.; Liu, S. *Angew. Chem., Int. Ed.* **2012**, *51*, 455−459.

(23) Liu, G.; Zhang, G.; Hu, J.; Wang, X.; Zhu, M.; Liu, S. *J. Am. Chem. Soc.* **2015**, *137*, 11645−11655.

(24) (a) Carl, P. L.; Chakravarty, P. K.; Katzenellenbogen, J. A. *J. Med. Chem.* **1981**, *24*, 479−480. (b) Alouane, A.; Labruere, R.; Le Saux, T.; Schmidt, F.; Jullien, L. *Angew. Chem., Int. Ed.* **2015**, *54*, 7492−7509. (c) Roth, M. E.; Green, O.; Gnaim, S.; Shabat, D. *Chem. Rev.* **2016**, *116*, 1309−1352.

(25) (a) Hu, X. L.; Hu, J. M.; Tian, J.; Ge, Z. S.; Zhang, G. Y.; Luo, K. F.; Liu, S. Y. *J. Am. Chem. Soc.* **2013**, *135*, 17617−17629. (b) Liu, G. H.; Wang, X. R.; Hu, J. M.; Zhang, G. Y.; Liu, S. Y. *J. Am. Chem. Soc.* **2014**, *136*, 7492−7497. (c) Wang, X. R.; Hu, J. M.; Liu, G. H.; Tian, J.; Wang, H. J.; Gong, M.; Liu, S. Y. *J. Am. Chem. Soc.* **2015**, *137*, 15262−15275. (d) Wang, L.; Liu, G. H.; Wang, X. R.; Hu, J. M.; Zhang, G. Y.; Liu, S. Y. *Macromolecules* **2015**, *48*, 7262−7272. (e) Li, Y. M.; Liu, G.

H.; Wang, X. R.; Hu, J. M.; Liu, S. Y. *Angew. Chem., Int. Ed.* **2016**, *55*, 1760−1764.
(26) Ikeda, M.; Tanida, T.; Yoshii, T.; Kurotani, K.; Onogi, S.; Urayama, K.; Hamachi, I. *Nat. Chem.* **2014**, *6*, 511−518.
(27) McBride, R. A.; Gillies, E. R. *Macromolecules* **2013**, *46*, 5157−5166.
(28) (a) Smith, D. A.; Cunningham, R. H.; Coulter, B. *J. Polym. Sci., Part A-1: Polym. Chem.* **1970**, *8*, 783−784. (b) He, L. H.; Read, E. S.; Armes, S. P.; Adams, D. J. *Macromolecules* **2007**, *40*, 4429−4438.
(29) Yang, Y. F.; Mijalis, A. J.; Fu, H.; Agosto, C.; Tan, K. J.; Batteas, J. D.; Bergbreiter, D. E. *J. Am. Chem. Soc.* **2012**, *134*, 7378−7383.
(30) (a) Ho, M. C.; Menetret, J. F.; Tsuruta, H.; Allen, K. N. *Nature* **2009**, *459*, 393−399. (b) Isom, D. G.; Castaneda, C. A.; Velu, P. D.; Garcia-Moreno, B. *Proc. Natl. Acad. Sci. U. S. A.* **2010**, *107*, 16096−16100.
(31) El-Sayed, M.; Kiani, M. F.; Naimark, M. D.; Hikal, A. H.; Ghandehari, H. *Pharm. Res.* **2001**, *18*, 23−28.
(32) Chen, C. Y.; Chen, C. T. *Chem. Commun.* **2011**, *47*, 994−996.
(33) Hu, X. L.; Liu, G. H.; Li, Y.; Wang, X. R.; Liu, S. Y. *J. Am. Chem. Soc.* **2015**, *137*, 362−368.
(34) Marrache, S.; Dhar, S. *Proc. Natl. Acad. Sci. U. S. A.* **2012**, *109*, 16288−16293.
(35) Men, Y.; Peng, F.; Tu, Y.; van Hest, J. C. M.; Wilson, D. A. *Polym. Chem.* **2016**, *7*, 3977−3982.
(36) (a) Chien, M. P.; Carlini, A. S.; Hu, D.; Barback, C. V.; Rush, A. M.; Hall, D. J.; Orr, G.; Gianneschi, N. C. *J. Am. Chem. Soc.* **2013**, *135*, 18710−18713. (b) Biswas, S.; Kinbara, K.; Niwa, T.; Taguchi, H.; Ishii, N.; Watanabe, S.; Miyata, K.; Kataoka, K.; Aida, T. *Nat. Chem.* **2013**, *5*, 613−620.

DOI: 10.1021/jacs.6b04115
J. Am. Chem. Soc. 2016, 138, 10452−10466